Article:

Improving a convection permitting model simulation of a cold air outbreak

Field P.R.[1*], Cotton R. J.[1], McBeath K.[1], Lock A.P.[1], Webster S.[1], Allan R.P.[2]

1: Met Office, Exeter, UK, 2: Department of Meteorology, University of Reading

*Correspondence to: paul.field@metoffice.gov.uk

A convection permitting local area model was used to simulate a cold air outbreak crossing from the Norwegian Sea into the Atlantic Ocean near Scotland. A control model run based on an operational configuration of the Met Office UKV high resolution (1.5 km grid spacing) NWP model was compared to satellite, aircraft and radar data. While the control model captured the large scale features of the synoptic situation it was not able to reproduce the shallow ($<$1.5km) stratiform layer to the north of the open cellular convection. Liquid water paths were found to be too low in both the stratiform and convective cloud regions. Sensitivity analyses including a modified boundary layer diagnosis to generate a more well mixed boundary layer and inhibition of ice formation to colder temperatures improved cloud morphology and comparisons with observational data. Copyright © 2012 Royal Meteorological Society

1. Introduction

Convection permitting models are being used routinely for operational numerical weather prediction. This approach can provide realistic realisations of convective events, their mesoscale organisation and propagation (Lean et al.

2008). Cold air outbreaks are challenging for such models because the depth of the boundary layer and the scale of the convection is approaching the resolution of the model. In addition, any cloud liquid is usually supercooled and so the accurate treatment of mixed-phase by the model is likely to

be important. Cold air outbreaks are a common phenomena around the United Kingdom. These potentially multi-day events can bring snow and the accuracy of a forecast will depend on the success of the simulation.

The case presented in this paper is a cold air outbreak that was observed on 31st January 2010. These are a common feature in the winter time to the north of the British Isles where cold air from the polar cap sweeps off the ice edge over open water. The convection often originates as organised rolls near to the ice edge but eventually changes into open cellular convection as the boundary layer evolves (see Brümmer and Pohlmann (2000) and references therein). These cloud morphological changes can have important impacts on the transport of heat and moisture as well as radiative effects such as high latitude Short Wave errors that are one of the largest biases in climate models (Karlsson and Svensson, 2010, Trenberth and Fasullo, 2010, Bodas-Salcedo et al. 2012). Accurate forecasts of such events are also important for civil aviation safety (e.g. Wilkinson et al. 2012).

Previous high resolution modelling studies of cold-air-outbreaks show roll formation and generally exhibit a boundary layer thickness of less than 1 km (e.g. Liu et al 2005, Gryschka and Raasch 2005). Both studies were idealised and concentrated on the early development of the cloudy boundary layer. The former study used a model capable of a multi-phase representation of water, while the second study did not have a cloud ice representation. Larger domain mesoscale modelling studies (e.g. Wacker et al. 2005, 7km grid resolution) of cold air outbreaks found broadly good agreement between modelled and observed boundary layer structure but the coarse grid resolution meant that the smaller scale convection remained unresolved.

A model intercomparison paper looked at the performance of a variety of single column and cloud resolving models in the stratiform region of a cold air outbreak during the Mixed-Phase Arctic Cloud Experiment (Klein et al. 2009). For that case the boundary layer was 1-1.5km deep (-15C at the top). Observed cloud liquid water paths were between 0.1-0.2 kg m^{-2}, while ice water paths were likely between 0.01-0.03 kg m^{-2} . Some models with complex microphysics were able to reproduce the liquid water path, but other models that produced low liquid water paths were only able to increase this value when ice processes were disabled. This led to the conclusion that there was excessive conversion of liquid to ice. Similar conclusions about the trade off between ice processes and liquid water path have been made by others studying arctic stratus cloud (e.g. Morrison and Pinto, 2006, Liu et al. 2011).

The aim of this paper is to compare a high resolution weather model simulation of a real case to insitu and remote sensing observations. This was done for a situation that is challenging to the model in terms of the grid resolution employed and the physics parametrizations. This case covers the evolution of a completely cloud covered shallow boundary layer through a transition to open celled convection. Changes to the physics representations will be made based on problems highlighted through comparison with the data. Finally, it will be determined if any of the changes that could easily be implemented in an operational forecast model led to an improved forecast.

2. Observations

2.1. Satellite data

Microwave based retrievals of liquid water path (LWP), integrated water vapour (WVP) and sea surface temperature (SST) are available from the AMSR-E (Advanced Microwave Scanning Radiometer) sensor on the AQUA/TERRA polar orbiting platforms. For this geographical region the data may suffer from systematic biases of the order of 15% (O'Dell et al. 2008) mainly due

to assumptions about partitioning of rain and cloud water. The LWP product is produced by Remote Sensing Systems (RSS) on a 0.25 degree grid and has an accuracy of 0.025 kg m^{-2} (Wentz et al. 1998). Horvath and Davis (2007) show agreement within 10% between LWP obtained using the Wentz (1998) product and other satellite measurements for boundary layer cloud with large cloud fractions but note a positive bias for lower cloud fractions. The overpass presented for this day occurred at 12:55 UTC. Top of atmosphere outgoing shortwave (SW) and longwave (LW) broadband radiative flux estimates are provided by the CERES instrument (Clouds and the Earth's Radiant Energy System) Single Scanner Footprint (SSF) processing system (version SSF_Aqua-FM3-MODIS_Version2F_008017) described in Wielicki et al. (1996). For overcast, moderate or thick low clouds over the ocean, Loeb et al. (2007) estimate an uncertainty in radiance to flux conversion of less than 5% for SW and less than 3% for LW. Given typical SW fluxes of up to 200 Wm^{-2} and LW fluxes of around 200 Wm^{-2} for the period of study, from the above uncertainty estimates we consider an accuracy of 10 Wm^{-2} for SW fluxes and 6 Wm^{-2} for the LW flux to be reasonable.

There was a MODIS (Moderate Resolution Imaging Spectroradiometer) overpass at 12.35 UTC on 31st January. MODIS level 2 data (http://ladsweb.nascom.nasa.gov/) provides retrievals of cloud top pressure, cloud top temperature, optical thickness and droplet effective radius. At this time of the year the solar zenith angle is large (∼80 degrees) and so there is a potential for bias in these retrievals.

2.2. Aircraft instrumentation

Observations, presented here, from a flight on 31st January 2010 were from the FAAM (Facility for Airborne Measurement) BAe-146 aircraft (see http://www.faam.ac.uk/index.php/science-instruments for details concerning standard meteorological variables such as winds, temperature and pressure). Instrumentation included a hot wire deep cone Nevzorov probe (Korolev et al. 1998) to mitigate problems with bouncing (Korolev et al. 2011) and a new calibration technique to provide condensed total water estimates to an accuracy of 0.001 g m^{-3} (Cotton et al. 2012) and saturates at ∼1 g m^{-3} (although it is noted that measured values during this flight did reach 2 g m^{-3}). The Nevzorov probe provided in-situ ice water content estimates (IWC). Cloud droplet number and sizing (2-50 microns) is provided by the laser scattering Cloud Droplet Probe (CDP, Droplet Measurement Technologies, USA). The CDP was used to provide in-situ liquid water content estimates (LWC) and was found to show good agreement with a liquid water hot wire probe. Ice crystals are measured using a Particle Measuring Systems 2D-C (25-800 microns) with modified tips (Korolev et al. 2011) and interarrival time filtering (Field et al. 2006) to reduce the effects of shattering on the measured size distribution. Ice properties such as ice number concentration are only derived from particles larger than 100 microns due to uncertainties with measuring and counting smaller particles. A Buck Research Instruments chilled mirror hygrometer provided relative humidity information.

2.3. Radar data

Radar data from the 3 GHz (C-Band) UK operational radar located on Stornaway was used to compare with model data as described in McBeath et al. (2012) that included clustering and tracking of cells. Model and radar data within 150 km of 58.2N, 6.2W and 09:30-14:00 UTC were processed. Combining radar data from 4 scan angles provided composite reflectivity fields at an altitude of ∼2km regridded onto the same resolution grid as the model data. A threshold of 10 dBZ was applied to the radar and model derived reflectivity fields at this height and histograms of convective cell size and shape were derived. For the radar data an individual convective cell is defined by a closed 10 dBZ reflectivity contour. Each identified

convective cell is enclosed by the smallest fitting circle. The diameter of this circle defines the convective cell size and the fraction of the circle occupied by the area enclosed by the 10 dBZ contour is termed the fill fraction.

3. Unified Model

The Unified Model is used at a variety of scales for climate prediction and Numerical Weather Prediction. The data presented here is from a nested high resolution model based on an operational UKV configuration (vn7.7, Parallel Suite 26). The global model (N512: 25km grid spacing at midlatitudes) was nested down through 12km, 4 km and 1.5km gridscale configurations of the UM. The 1.5km domain was 750 km (east-west) by 1500 km (north-south) In the vertical there are 70 levels stretched up to 40 km (52 below 10km, 33 below 4km, 16 below 1km) and the timestep is 50s. Lateral boundary conditions are updated at 1 hourly intervals to the 12 and 4km nests and half hourly intervals to the 1.5km nest. There is no convection scheme in the 4 and 1.5 km gridscale models, the model handles convection at the grid scale.

Mixing is handled in the vertical by a non-local 1-D boundary layer scheme. Lock et al (2000) describe the boundary layer scheme in the UM that generates a diagnosis of boundary layer "type" based on the surface buoyancy flux and profiles of potential temperature, winds and humidity. The boundary layer type determines the non-local mixing throughout the lower troposphere. If the environment is diagnosed to be conditionally unstable (i.e., capped by cumulus clouds) then vertical mixing in the cloud layer is assumed to be resolved and the boundary layer parametrization mixes only to the lifting condensation level [*].

The Unified Model cloud microphysics is a single moment, three phase representation. For the liquid phase there are prognostic variables for cloud water and rain mixing ratio. For ice there is a prognostic variable for snow mass mixing ratio that represents all ice in the grid box. Production of cloud water is through condensation and loss occurs through droplet settling, autoconversion of droplets to rain, freezing of droplets by ice nucleation and riming. Production of rain mixing ratio is via autoconversion, accretion and melting of ice. Loss of rain mixing ratio is from evaporation, capture by ice and homogeneous ice nucleation. Sedimentation can lead to loss or gain of rain. Ice mixing ratio production is from diffusional growth, capture of rain and riming. Loss of ice mixing ratio comes from sublimation and melting. Sedimentation acts on the ice mixing ratio. The basic formulation is described in Wilson and Ballard (1999) [†]

Of direct interest here is that heterogeneous ice nucleation occurs when the temperature is colder than -10C and liquid water is present. The control snow size distribution representation is an exponential distribution based on the Houze et al. (1979) observations. There is an additional diagnostic split of the ice mixing ratio between ice crystals and snow that is a function of the depth below cloud top. This provides a steeper distribution of small crystals that sediment slower (see Cotton et al. 2012 for a fuller description). At each time step the ice mixing ratio is diagnosed into 'ice' and 'snow' the process rates are computed for each and then they are summed to provide the combined effect.

A cloud scheme deals with subgrid humidity variations (Smith 1990). The model is nonhydrostatic and uses a semi-Lagrangian dynamical formulation (Cullen et al. 1997, Davis et al. 2005). For the liquid phase, the radiation

---

[*]Full documentation is also available from the Met Office: Unified Model Documentation Paper 24 The Parametrization of Boundary Layer Processes, A Lock 2011. http://collab.metoffice.gov.uk/twiki/pub/Support/Umdp/024_79.pdf

[†]Full documentation is also available from the Met Office: Unified Model Documentation Paper 26 The Large-Scale Precipitation Parametrization Scheme J Wilkinson 2011. http://collab.metoffice.gov.uk/twiki/pub/Support/Umdp/026_77.pdf

scheme assumes a constant droplet number (100 cm^{-3} over ocean) and combines this with the liquid water content to compute an effective radius for use in the short wave calculations. For the long wave a constant effective radius of 7 microns for droplets is assumed. There is also a heterogeneity factor (0.7) to account for the effects of cloud structure on the radiation field. More details of the unified model can be found in Walters et al. (2011) and references therein, including details about the global model analysis used to initialise this case study. The data presented here is from a 30 January 2010 12UTC run initialised from archived global analyses. The 1.5km nested run began 6 hours later and runs from 18 UTC 30th January 2010 through to the end of 31st January 2010. The comparisons are made with observations during the 31st January.

4. Results

4.1. Comparison with control model

In this section the observations are introduced and compared to the control model (**h**). Based on any deficiencies identified changes to the microphysical representation were made and their similarity to the observations is discussed. It was noted that the position of synoptic features at 13UTC was better matched to the model at 11UTC. Therefore, for the comparisons of WVP and LWP those times were used. For the SW and LW, 12 UTC was used.

4.1.1. Synoptic situation

Figure 1 shows the 12UTC analysis for 31 January 2010. This general synoptic pattern persisted from the 29 January until 1st February. There was a strong northerly flow that extended from latitudes higher than 70N to the southern tip of the British Isles. A polar low feature was present near 68N 4E (also see location in fig 2b) that constricted the flow to the east of Iceland. Further into the Atlantic

there was a warm front to the southwest of Iceland that had a cirrus shield ahead of it. The large scale sea level pressure pattern is very similar to the composite produced by Kolstad et al. (2009) for strong marine cold air outbreaks in this region. MODIS radiance imagery from a visible channel 4 (545-565nm, fig. 2a) and infrared channel 31 (10.78-11.28μm, fig. 2b) shows the overrunning cirrus from this warm front. This cirrus can be seen as lighter regions in figure 2b to the west of 12W meridian. North of 64N, the cirrus extends further eastwards to 6W. The polar low is a clear cyclonic feature in the cloud fields. Between 12W-6W and 60N-64N there is low cloud exhibiting nearly complete cloud cover. South of this the cloud breaks up into open cellular convection.

4.1.2. Satellite comparison

Examining the performance of the control model (fig 2c) shows that it exhibits gross similarities with the satellite observed cloud morphology (fig. 2a,b, irradiance and radiances are compared only to assess the gross cloud structures). The incoming cirrus shield, polar low and open cellular convection near Scotland are captured, but the stratiform cloud with cloud fraction close to 100% between the polar low and Iceland is absent. This is replaced in the simulation by broken convective cloud. In figure 3a,e intergrated water vapour path (WVP) shows good agreement between model and observations, with the polar low feature drawing in dry air from the north associated with the polar low feature clearly visible. Figure 3b shows the LWP from AMSR-E peaked to the west of the Faroe Islands with a value of 0.3 kg m^{-2} extending towards Iceland. Outside of this region the LWP values are 0.05 kg m^{-2} in the regions of low cloud to the north and the convective cloud region to the south. The control model exhibits very little liquid water when compared to the observations (fig. 3 b,f). The largest values are associated with the polar low feature and the deeper convection towards the southern part of the domain. Top

of atmosphere outgoing LW radiation from the model is too great, indicating that there is not enough cloud, leaving the LW flux to be strongly affected by emission from the surface (fig. 3c,g). The top of atmosphere outgoing SW flux is affected in the north east of the domain by the terminator, but it is still clear that the lack of cloud cover in the stratiform region means that the SW flux at the top of the atmosphere is reduced when compared to the observations (fig. 3d,h).

Averaging MODIS level 2 retrievals over a 100km box centred on 62N 10W (see fig. 2b) indicates a cloud water path of 0.3 $\pm$0.2 kg m^{-2} in agreement with the microwave retrieval. In addition a cloud top temperature and pressure of -14 $\pm$2 C and 760 $\pm$30 mb for the stratiform cloud in this region. Assuming a surface pressure of 1004 mb cloud top height is then 2180$\pm$300 m. Finally, following Boer and Mitchell (1994) the retrieved droplet effective radius and optical thickness can be combined to obtain an effective droplet concentration. The value obtained is 110 $\pm$ 160 cm^{-3}. An error of a factor of 10 in optical thickness would lead to an error in concentration of a factor of $\sim$ 3. The lack of stratiform cloud in the control model at this location means that no meaningful comparisons can be made the control model and the MODIS derived values.

4.1.3. Aircraft comparison

Model comparisons have been carried out by coarse-graining the model fields into 100 km squares and then comparing mean and standard deviations to the aircraft observations. In-cloud statistics were computed using only grid boxes where the condensed water mixing ratio exceeded 10^{-8} kg kg^{-1}. The fraction of grid boxes at each height exceeding this threshold within a 100km x 100km box is called the cloud fraction. A square region centred on 8W, 58N was chosen for comparison with the observations based on the region where the aircraft had flown and by assessing how well the relative humidity, temperature and

horizontal wind profiles matched the observed values (this region is displaced $\sim$50km southwest of where the aircraft flew). The control model is able to reproduce the horizontal winds and temperature profiles but is not able to capture the large humidity values observed by the aircraft and dropsondes between 2000–2700m.

In-situ evidence for a lack of liquid water was provided from the aircraft measurements. The FAAM Bae-146 research aircraft penetrated cumulus clouds from 10UTC to 15UTC in a region approximately bounded by 8W-6W and 58N-60N in a series of $\sim$50 km straight and level runs through the cumulus cloud. Downward looking LIDAR from runs carried out at an altitude of 6 km indicated cloud top at 3.7 km. Cloud base was observed to be at 1 km. Precipitation was observed to be reaching the surface and the freezing level was at 0.5km. One cell was followed up from 2 km where it was mixed-phase to 3 km where it had completely glaciated. The clouds were observed to have liquid cores with ice outflows. Figure 4 shows vertical profiles of humidity, temperature, potential temperature and horizontal winds from two dropsondes launched by the aircraft at 10:37UTC and 14:22UTC and aircraft measurements from straight and level legs between those times (mean and one standard deviation shown). Relative humidity from the aircraft exhibits large variability encompassing the dropsonde data and ice saturation between 2.0-2.6km (fig. 4a). Temperature from the aircraft shows good agreement with the sondes between 1.5-2.6km and the freezing level is indicated to be between 200-500m (fig. 4b). Potential temperature shows that the aircraft derived values exhibit less variation with height than the sondes (fig 4c). Horizontal winds are only available from the aircraft up to 2km. Icing up of the pitot tubes has affected measurements above this altitude. Again, the aircraft measurements compare well with the dropsonde values indicating a 14–17 m s^{-1} northerly and 2–6 m s^{-1} westerly between 500m and 2000 m altitude (fig 4d,e).

In-cloud condensed water estimates from the Nevzorov (IWC) and CDP (LWC) show that clouds were sampled between 1.5-2.6km (fig. 5). Mean in-cloud IWC and LWC increased in altitude up to 0.7 and 0.6 g m^{-3}, respectively. Some low values of LWC can be seen near 2.5 km indicating that the cloud had become almost completely glaciated. Greater values at the same altitude indicate that it is also the case that some clouds were not yet glaciated. LWC and IWC values measured by the aircraft were generally comparable in magnitude. Droplet concentrations measured by the CDP have mean values of 10 cm^{-3} and no obvious height dependency (fig 6a). Inspection of cloud thickness, fraction and in-cloud LWC (fig 5) suggest a LWP of ~0.05 kg m^{-2}, consistent with the microwave based satellite retrieval for this region. Ice with maximum dimensions greater than 100 microns exhibit concentrations that increase in height to mean concentrations of 20 L^{-1} at 2.6 km (fig. 6b). The greatest mean in-cloud concentration at this altitude (T=-18C) is 50 L^{-1}. The averaging in-cloud lengths for each run was typically 10-20km for ice and 1-10km for the liquid regions reflecting the smaller extent of supercooled liquid water. Thresholds of 2 cm^{-3} and 0.01 L^{-1} on the CDP and 2D-C, respectively, were used as thresholds for computing liquid and ice in-cloud water contents.

In-cloud ice water contents for the control model (black solid line, fig. 5a) are below the lowest measured values. We note that the measured IWC values are close to the upper limit of the Nevzorov probe and therefore IWC values may be greater than depicted. Similarly, the liquid water content from the control model is well below the observed values (fig. 5b), and ice and liquid cloud fraction are low for the control model when compared to the aircraft estimates (not shown). The model assumes a drop concentration of 100 cm^{-3} and so does not feature on figure 6a. Comparison of ice concentration for particles larger than 100 microns (fig. 6b) indicates that the simulations using the control model representation diagnose ice concentrations similar

to the measured values. Microphysical process rates can be expressed in terms of the moments of the ice particle size distribution (PSD), $N(D)$, where the nth moment is defined as $M_n = \int D^n N(D) \mathrm{d}D$. In terms of microphysical processes the diffusional growth is approximately determined by the first moment of the size distribution [‡]. For the control representation the first moment for particles larger than 100 microns is again in agreement with the observations from the aircraft (fig. 6 c). Because radar reflectivity is proportional to the square of the mass of a particle and in turn the mass is approximately proportional to the square of the size, therefore, the fourth moment of the ice size distribution is proportional to the radar reflectivity. It can be seen in figure 6d that the control model underpredicts the aircraft derived values.

4.1.4. Radar comparison

Convective cell identification, using a 10 dBZ threshold, and tracking were used to ascertain convective cell lifetime and size. Mean convective cell lifetime from the radar is 69 minutes (3 minute standard error) compared to 65 minutes (6 minute standard error) for the control. Histograms of convective cell size (fig 7a), fill fraction (fig 7b) and maximum reflectivity in a convective cell (fig. 7c) are shown. The control model, (**h**), exhibits larger convective cell sizes and the fill fraction derived from the model was greater than the value derived from the radar data. Thus the convective cells derived from the model appear rounder than they are in the observations. Histograms of maximum reflectivity within a convective cell at this altitude indicates that the control model has a similar distribution of reflectivity values to the radar data.

4.1.5. Summary of Control model performance

From comparison with aircraft, radar and satellite data several problems have been identified with the control

---

[‡] ventilation effects will lead to diffusional growth being proportional to a higher order moment between 1 and 2.

model for this case. i) There is too little condensed water. In particular the liquid water content is too low, and hence liquid water path, in both the stratiform region and the convective region is underpredicted. ii) The cloud cover in the stratiform region is too broken. iii) The reflected SW (emitted LW) at the top of the atmosphere is too little (great) which is likely to be the result of the combination of points i) and ii). iv) In the convective region the fourth moment of the ice size distribution is underpredicted suggesting that the ice size distribution is too narrow. v) The convective cell sizes for the control model are too large and the model derived fill fractions are too high.

4.2.   Sensitivity tests

Shortcomings in the control model motivated a number of variations to the physics representation. These changes are described here and the different model configurations that combine these changes are given in table 1.

Shear dominated boundary layer:. This change was motivated by the lack of stratiform cloud between the polar low and Iceland. As described in section 3, the boundary layer scheme in the UM provides a diagnosis of boundary layer "type" based on the surface buoyancy flux and the thermodynamic profile characteristics that determines the non-local mixing throughout the boundary layer. If the environment is diagnosed to be conditionally unstable then vertical mixing is assumed to be resolved and the boundary layer scheme does not handle the mixing above the lifting condensation level. This was the case in the control model and meant that it was difficult to achieve the 100% cloud cover in the stratiform region indicated by the satellite observation. It was hypothesised that the large vertical shears experienced in these regions were not being dealt with properly. Shear generation of turbulence can extend mixing into regions of weak static stability. To allow for this effect additional dynamical constraints were added that can allow the boundary layer schemes non-local diffusion profiles to parametrize the mixing right up to

cloud top. This diagnosis is made by inspection of the local Richardson number profile - if this is less than 0.25 from the surface to at least the mid-point of the cloud layer then wind shear is assumed to disrupt the formation of cumulus clouds and the boundary layer scheme diagnoses a more appropriate well-mixed stratocumulus topped boundary layer (see Bodas-Salcedo et al. 2012 for additional details).

Tnuc=-18C: The lack of liquid water in the control model led to the hypothesis that the production of ice was too efficient. Currently, in common with other operational microphysics schemes, the model produces ice through heterogeneous freezing when the temperature is -10C or colder and liquid water is present. This represents a condensation or immersion freezing mechanism. Changing the primary heterogeneous ice nucleation temperature from -10 to -18C inhibits ice production until the boundary layer top approaches about 4km. Using a colder heterogeneous freezing temperature is supported by both laboratory and remote sensing observations (Field et al. 2006, Ansmann et al. 2008, Westbrook et al. 2011). In addition to the nucleation temperature change, no ice below 4 km is allowed to enter through the boundaries. Any ice entering the boundary or in the initial model fields was converted to liquid water. This was done to avoid contamination by ice from the coarser nest domains and initial fields without having to rerun the entire suite. It is noted that for these ice inhibition sensitivity experiments the upper level cirrus will not fully recover during the course of the simulation because of the initialisation.

No Ice: A more extreme inhibition of ice formation. All the ice processes were eliminated and any existing ice in the initial conditions was converted to liquid (including a latent heat correction).

AcE=0.1: The lack of liquid water led to the hypothesis that the production of precipitation through autoconversion was too efficient. The operational UM uses the Tripoli

Table 1. Model variations. For brevity the different configurations are referred to by their last letter in the text). The control model is dimsh.

Experiment	Sh. dom. BL.	Tnuc=-18C	AcE=0.1	No ice	PSD	3dSmag
dims**h**						
dims**p**				✓		
dims**q**			✓			
dims**n**						✓
dims**k**	✓					
dims**i**	✓		✓			
dims**z**	✓	✓				
dims**y**	✓	✓	✓			
dims**u**	✓	✓	✓		✓	
dims**w**		✓	✓			✓

and Cotton (1980) formulation of autoconversion. The autoconversion efficiency is usually set to 0.55, but for this sensitivity the value was change to 0.1 to reduce the transfer of cloud water to precipitation.

3dSmag: It was hypothesised that water may be mixed more efficiently throughout the boundary layer if the model was able to do the mixing explicitly. Instead of using the boundary layer scheme to do the vertical mixing, local explicit mixing using the Smagorinsky approach (1963) was used (asymptotic mixing length 375m).

PSD: The aircraft observations showed that some properties of the ice/snow size distribution were not well represented (the UM has a single prognostic to represent ice and aggregates of ice: snow). The ice/snow representation is changed from the standard exponential representation (Wilson and Ballard, 1999) to one that was derived from a more extensive range of aircraft observations (Field et al. 2007).

4.3. Comparison with sensitivity tests

4.3.1. Satellite comparison

Table 2 contains sub-domain averages for the different experiments, restricted to the bottom right of the domain (east of 12W and south of 64N, see figure 3) to exclude the Cirrus cloud affected by initialisation for the ice inhibited sensitivity experiments. For the LWP, reducing

the occurrence of ice has the greatest effect. The total removal of ice processes (p) produces LWP values of a similar magnitude to the satellite observation in the stratiform and convective region, but produces very unrealistic results around the polar low feature (not shown) resulting in a positive mean bias. The change in the heterogeneous freezing temperature increases the LWP ((**k,z**)) in the stratiform region but not as much as removing all ice processes. Reducing the autoconversion on top of the freezing temperature change also increases LWP slightly further ((**z,y**)). Changing the ice PSD allows more supercooled liquid water to persist (**u**). SW and LW flux biases in table 2 show improvement when the *Shear dominated boundary layer* is used ((**h,k**)). Combining *Tnuc-18C* with the *Shear dominated boundary layer* does not lead to further significant improvements. The *No ice* experiment seems to remove the bias in SW and LW, but this is because overly bright cloud associated with the polar low feature compensates for the stratiform region being too dim. Finally it is noted that the assumed droplet number of 100 cm^{-3} is in agreement with the retrieval from MODIS, but it is greater than was observed in the convective cloud. Changing to a lower concentration will decrease the SW at the top of the atmosphere back towards the control values. However, the underestimate of the liquid water and cloud fraction by the model are the dominant factors for the radiation.

Changes to the model physics representations led to improved cloud cover, liquid water paths and associated radiative fluxes. However, while the sensitivity experiments that involve changes to the boundary layer (all apart from **h,q**) produce improved SW and LW results, they are difficult to decide between given the uncertainty in the observed values. Sensitivity experiment **u**, that included the PSD change, did better with the LWP and, as will be seen, characteristics of the ice size distribution within the convective cloud. Additional changes to assumptions within the SW radiation scheme could further reduce these biases, but the first order change to the SW response is associated with the increase in stratiform cloud cover. It has been decided to weight the improvements to LWP greater than those to the radiation, and therefore, the comparisons shown in figures 2, 3, 4, 8, 9 that will be discussed next show results from the control model **h** and the favoured sensitivity experiment **u**.

Figure 3 shows a comparison of the **u** model from table 1 with satellite derived liquid water path, top of atmosphere SW and LW fluxes. All of the fields are smoothed with a 100 km top hat filter. As before, the integrated water vapour path (3a,i) are similar, but now the liquid water path exhibits much greater values with a peak exceeding 0.2 kg m^{-2} (fig. 3j). Increases in cloud fraction mean that the LW flux (fig. 3k) is reduced relative to the control model (fig. 3g) and closer to the satellite derived value. The increased cloud cover leads to increased SW flux (fig. 3h,l) relative to the control model.

The presence of extensive stratiform cloud at 62N 10W allows a comparison to be made between the model fields and the MODIS retrievals. For the **u** sensitivity experiment the mean values obtained for the 100km x 100km box (mean followed by standard deviation in brackets) are -16(1)C compared to -14(2)C from MODIS for cloud top temperature, 770(20)mb compared to 760(30)mb from MODIS for cloud top pressure, 1970(180)m compared

to 2180(300)m from MODIS for cloud top height and 0.15(0.1) kg m^{-2} compared to 0.3(0.2) kg m^{-2} from MODIS for liquid water path.

4.3.2. *Aircraft comparison*

Inhibiting ice production to colder temperatures is required to increase the model LWC. Only the experiment where ice has been switched off **(p)** approaches the observed LWCs (fig. 5b); when ice is present it inhibits the liquid in the stratiform cloud and elsewhere. The contrast between the good agreement between the predicted and measured ice properties in this convective region and the difficulties with reproducing the LWC leads to the suggestion that when liquid and ice are present in a grid box there is not enough physical separation of these two phases. That is to say, the two phases are assumed to be well mixed throughout a grid box and in contact via the vapour phase for the Wegener-Bergeron-Findeisen mechanism to operate and able to collide with each other. Both these processes efficiently remove the liquid phase from the grid box.

The boundary layer changes increase both in-cloud IWC (fig. 6a, **k,y,u**) and ice fraction (not shown) to values comparable to the observations even though the impact of that change is far upstream. Comparison of ice concentration and the first moment of the ice size distribution for particles larger than 100 microns indicates that the simulations using the standard representation (fig 6b,c **h, k, y**) diagnose values comparable to the observations. The new PSD representation produces better agreement with the fourth moment of the ice size distribution (fig. 6d), indicating that the observed PSD was much broader than the control model representation for this case.

Table 2. Model biases. Mean of (experiment-observations) from box depicted in figure 3.

Experiment	LWP [kg m^{-2}]	SW [W m^{-2}]	LW [W m^{-2}]
Obs. mean	0.042	135	214
dimsh	-0.029	-22	11
dimsp	0.101	2	1
dimsq	-0.030	-22	12
dimsn	-0.030	-13	6
dimsk	-0.028	-8	5
dimsi	-0.029	-8	5
dimsz	-0.021	-10	6
dimsy	-0.017	-9	5
dimsu	-0.014	-8	7
dimsw	-0.019	-10	5

4.3.3. Radar comparison

For simplicity only a subset of the results have been shown. Comparing convective cell sizes (defined by the 10 dBZ reflectivity contour) shows that most experiments exhibit greater frequencies of larger convective cell sizes (>20km) than the radar (fig. 7a). Experiments **(h,q), (k,i), (z,y)** differ through the change to the Autoconversion and result in increases in the occurrence of convective cells with greater fill fractions (not shown). Looking at the effect of inhibiting the ice production process experiments **(h,p)** and **(k,z)** (not shown) indicate that the convective cell sizes tend to decrease and the maximum reflectivities increase. Experiments **(k,n) (y,w)** show little change when Smagorinsky mixing is used in the vertical. Changing the ice PSD **(y,u)** resulted in smaller convective cell sizes and decreased occurrence of maximum reflectivity greater than 30 dBZ.

4.3.4. Lagrangian profiles

It is easier to understand how the boundary layer is evolving by tracking a region in an approximately Lagrangian way. A region was advected with a mean model wind (averaged below 1.5km) within a 100 km x 100 km domain, by simple forward stepping in time, from 66N,11W at 0UTC to 57N, 6W, at 15 UTC (fig. 2b). Inspection of model profiles within the stratiform part of the cloud at 0430 UTC provides an assessment of the impact of the sensitivity experiments. The experiments that differ only by the change in autoconversion (**(h,q), (k,i), (z,y)**) do not exhibit much change in liquid fraction or liquid water content. The shear driven boundary layer change (**(h,k)**) leads to increased liquid cloud fraction but not liquid water content. When the ice processes are switched off or inhibited (**(h,p), (k,z)**) the liquid water content and fraction is greatly increased. For both the switching off of ice and the change to the boundary layer mixing the net flux of moisture through cloud base will increase. Using *3dSmag* (**(k,n), (y,w)**) also leads to increases in both liquid cloud fraction and content, but not to the same extent that inhibiting the ice does. The *3dSmag* experiments also gives rise to a lower boundary layer top than those using the *Shear dominated boundary layer*, probably due to the poor resolution leading to less efficient entrainment.

Mean vertical profiles (fig. 8) shows the boundary layer growing from 1.5km at 0 UTC to 3 km at 14:30 UTC. The control (h) has a lower boundary layer top and exhibits less well mixed profiles of potential temperature and total water than the favoured sensitivity experiment shown (u). This results in drier profiles (fig. 8d), lower cloud fractions (fig. 9) and less condensed liquid water (fig 8c) than the experiment. The effect of changing the treatment of the boundary layer either through the *Shear dominated boundary layer* or using *3dSmag* (not shown) for the vertical mixing was to create a more well mixed boundary layer, evident in the potential temperature and

total water plots (fig. 9 a,b). The relative humidity profiles for the experiment are much closer to water saturation (also see fig. 4a) and condensed water amounts are increased. Time evolution of the liquid and ice cloud fraction shows that the experiment is able to evolve from 100% liquid cloud cover early on to greater fractions of ice cloud later on (fig. 9). In contrast, the control model exhibits generally decreasing ice and liquid cloud fraction with time.

5.   Discussion

Stratiform cloud poleward of the open cellular convection is a common feature of cold-air-outbreaks (e.g. Brümmer and Pohlmann 2000). The lack of this cloud in the control 1.5km run highlights the difficulty even convection permitting models have with representing cloud systems with shallow boundary layers. The modification of the boundary layer scheme to recognize that a shear dominated boundary layer will result in a stratocumulus topped boundary layer led to an improved representation in terms of cloud coverage and outgoing top of atmosphere SW flux. This change also allowed the model to capture the transition from stratiform cloud to open celled convection. Such an approach was also implemented in a global model leading to better representation of this cloud type around midlatitude cyclones (Bodas-Salcedo et al. 2012). However, even with the boundary layer modification, the liquid water path from the model was much smaller than that estimated from the satellite retrieval. Model derived liquid water paths only approached similar values to those reported by the satellite measurements when the temperature at which ice is produced by heterogeneous freezing was lowered from -10C to -18C. This meant that ice did not form until the boundary layer had grown towards 4km and the cloud had broken up into cellular convection. For this case, even the reduction in the ice production was not sufficient to match the aircraft observations of supercooled liquid water content. Only an unrealistic suspension (*No Ice*) of ice processes was able to produce liquid water content profiles

that matched the aircraft observations.

The improvement of liquid water content through the inhibition of ice processes is a result reported by others (e.g. Klein et al. 2009) and has implications for other microphysics schemes that use a heterogeneous ice onset temperature around -10C. However, simply setting the freezing onset temperature in the operational UK model to -18C may result in adverse results, due to the lower precipitation efficiency of shallow winter time showers, and needs to be tested further. The colder onset temperature may just be a result of a rarer occurrence of ice nuclei in air from the arctic than airmasses arriving from Europe. This proposition provides motivation for testing cold air outbreak cases with an aerosol-cloud interactive NWP suite.

The liquid water contents were still too low for the sensitivity test with the modified boundary layer, colder freezing temperature and modified PSD (**u**). This raises the possibility that the well mixed assumption between liquid and ice phases is not correct. In the Unified Model there is a cloud phase overlap which determines how efficient riming and the Wegener-Bergeron-Findeisen process will be. For this modelled case, the ice and liquid phases are in maximum contact through the vapour phase and the potential to rime. The *No Ice* test shows that if it was possible to shield the liquid phase from the ice phase within a grid box then the correct liquid water paths could be generated for the stratiform and convective cloud region, but not the polar low feature. More work needs to be done on determining how to parametrize the mixed-phase characteristics in these convection permitting models. It is clear that updrafts greater than a few metres per second will be sufficient to lead to a plume of liquid-only cloud surrounded by ice. It may be possible to use high resolution (decametre grid spacing) cloud resolving model studies to help derive a parametrization to represent this behaviour.

Modifying the boundary layer scheme to recognise a shear dominated boundary layer and decreasing the heterogeneous freezing temperature produced model results that improved upon those from the control model for SW and LW fluxes. The sensitivity experiment **u**, that included the change to the ice PSD, also improved the LWP and characteristics of the ice size distribution within the convective cloud. Because of the assumptions in the radiation scheme more weight was given to the quantitative improvements in LWP and insitu aircraft observations. The **u** configuration that incorporated the modified boundary layer scheme, the change in the onset of heterogeneous freezing to colder temperatures, the reduction in autoconversion efficiency and the new snow PSD was felt to produce the best simulation. Figure 2 shows a comparison of LW flux at the top of the atmosphere from the original control model (h), the MODIS infrared channel and the **u** sensitivity experiment, noting that the lack of cirrus is due to the initialisation used for this experiment.

6. Conclusions

From this study we can draw the following conclusions for the representation of cold air outbreaks by a 1.5km model. i) The favoured sensitivity experiment (**u**) evolves a shallow boundary layer stratiform cloud into a deeper boundary layer with open cellular convection producing better agreement with the observations than the control model. ii) Using a non-local mixing boundary layer scheme to implicitly represent a shear dominated boundary layer as a stratocumulus topped layer appears successful. This treatment reproduces the $\sim$100% cloud cover exhibited by the stratus layer and enhances the SW TOA flux. iii) A temperature of -10C for the onset of ice formation is too warm. This is presumably because of the clean nature of the airmass originating in the arctic and the lack of efficient ice nuclei available. A colder temperature onset for heterogeneous ice production improved liquid water

contents. iv) The model representation of mixed-phase is too efficient at removing liquid.

7. Acknowledgements

8. References

Ansmann, A, Tesche, M, Althausen, D; et al. 2008. Influence of Saharan dust on cloud glaciation in southern Morocco during the Saharan Mineral Dust Experiment. J. Geophysical Research-Atmospheres, 113 (D4): Art. No. D04210.

Bodas-Salcedo, A., K. D. Williams, P. R. Field, A. P. Lock, 2012: The Surface Downwelling Solar Radiation Surplus over the Southern Ocean in the Met Office Model: The Role of Midlatitude Cyclone Clouds. J. Climate, 25, 7467?7486.

Brümmer, B and Pohlmann, S, 2000: Wintertime roll and cell convection over Greenland and Barents Sea regions: A climatology. Journal of Geophysical Research-Atmospheres. 105, D12, 15559-15566, 10.1029/1999JD900841

Cotton, R. J., Field, P. R., Ulanowski, Z., Kaye, P. H., Hirst, E., Greenaway, R. S., Crawford, I., Crosier, J. and Dorsey, J. (2012), The effective density of small ice particles obtained from in situ aircraft observations of mid-latitude cirrus. Q.J.R. Meteorol. Soc.. doi: 10.1002/qj.2058.

Cullen M. J. P., T. Davies, M. H. Mawson, J. A. James, S. C. Coulter, and A. Malcolm, 1997: An overview of

numerical methods for the next generation UK NWP and climate model. Numerical Methods in Atmospheric and Ocean Modelling: The Andre J. Robert Memorial Volume, C. A. Lin, R. Laprise, and H. Ritchie, Eds., Canadian Meteorological and Oceanographic Society, 425-444.

Davies T., M. J. P. Cullen, A. J. Malcolm, M. H. Mawson, A. Staniforth, A. A. White, and N. Wood, 2005: A new dynamical core for the Met Office's global and regional modelling of the atmosphere. Quart. J. Roy. Meteor. Soc., 131, 1759-1782.

Field, P. R. and Heymsfield, A. J. and Bansemer, A., 2006: Shattering and particle interarrival times measured by optical array probes in ice clouds. Journal of Atmospheric and Oceanic Technology, 23, 10, 1357-1371, 10.1175/JTECH1922.1

Field, P.R., Mohler, O, Connolly, P, Kramer, M, Cotton, R, Heymsfield, A.J., Saathoff, H., Schnaiter, M., 2006: Some ice nucleation characteristics of Asian and Saharan desert dust. Atmospheric Chemistry and Physics 6, 2991-3006.

Field, Paul R.; Heymsfield, Andrew J.; Bansemer, Aaron, 2007: Snow size distribution parameterization for midlatitude and tropical ice clouds. JOURNAL OF THE ATMOSPHERIC SCIENCES, 64(12), 4346-4365 DOI: 10.1175/2007JAS2344.1

Gryschka, M and Raasch, S, 2005: Roll convection during a cold air outbreak: A large eddy simulation with stationary model domain. Geophysical Research Letter, 32, 14, 10.1029/2005GL022872

Horvath, A., and R. Davies (2007), Comparison of microwave and optical cloud water path estimates from TMI, MODIS, and MISR, J. Geophys. Res., 112, D01202, doi:10.1029/2006JD007101.

Karlsson, J., and G. Svensson, 2010: The simulation of Arctic clouds and their influence on the winter surface temperature in present-day climate in the CMIP3 multi-model dataset. Clim. Dyn., DOI 10.1007/s00382-00010-00758-00386.

Klein, Stephen A. and coauthors, 2009: Intercomparison of model simulations of mixed-phase clouds observed during the ARM Mixed-Phase Arctic Cloud Experiment. I: Single-layer cloud. Quarterly Journal of the Royal Meteorological Society, 135, 641, 979-1002, 10.1002/qj.416

Kolstad, Erik W. and Bracegirdle, Thomas J. and Seierstad, Ivar A.,2009: Marine cold-air outbreaks in the North Atlantic: temporal distribution and associations with large-scale atmospheric circulation, Climate Dynamics, 33, 2-3, 187-197, 10.1007/s00382-008-0431-5

Korolev, A. V. and Emery, E. F. and Strapp, J. W. and Cober, S. G. and Isaac, G. A. and Wasey, M. and Marcotte, D., 2011: Small Ice Particles in Tropospheric Clouds: Fact or Artifact? Airborne Icing Instrumentation Evaluation Experiment. Bulletin of the American Meteorological Society, 92, 8, 967-973, 10.1175/2010BAMS3141.1

Korolev, AV and Strapp, JW and Isaac, GA and Nevzorov, AN.1998:The Nevzorov airborne hot-wire LWC-TWC probe: Principle of operation and performance characteristics. Journal of Atmospheric and Oceanic Technology, 15, 6, 1495-1510, 10.1175/1520-0426(1998)015¡1495:TNAHWL¿2.0.CO;2

Lean Humphrey W.; Clark Peter A.; Dixon Mark; et al., 2008: Characteristics of high-resolution versions of the Met Office Unified Model for forecasting convection over the United Kingdom. Monthly Weather Review, 136(9),

3408-3424.

Liu, A.Q., G. W. K. Moore, K. Tsuboki and I. A. Renfrew, 2006: The effect of the sea-ice zone on the development of boundary-layer roll clouds during cold air outbreaks. Boundary-Layer Meteorology 118: 557?581.

Liu, Xiaohong and Xie, Shaocheng and Boyle, James and Klein, Stephen A. and Shi, Xiangjun and Wang, Zhien and Lin, Wuyin and Ghan, Steven J. and Earle, Michael and Liu, Peter S. K. and Zelenyuk, Alla. 2011: Testing cloud microphysics parameterizations in NCAR CAM5 with ISDAC and M-PACE observations. Journal of Geophysical Research-Atmospheres, 116, 10.1029/2011JD015889

Lock A. P., A. R. Brown, M. R. Bush, G. M. Martin, and R. N. B. Smith, 2000: A new boundary layer mixing scheme. Part I: Scheme description and single-column model tests. Mon. Wea. Rev., 128, 3187-3199.

Loeb et al. 2007 J. Atmos. Oceanic Technol., 24, 564-584. Angular Distribution Models for Top-of-Atmosphere Radiative Flux Estimation from the Clouds and the Earth.s Radiant Energy System Instrument on the Terra Satellite. Part II: Validation doi: http://dx.doi.org/10.1175/JTECH1983.1

Morrison, H. and Pinto, J. O., 2006: Intercomparison of bulk cloud microphysics schemes in mesoscale simulations of springtime Arctic mixed-phase stratiform clouds. Monthly Weather Review, 134, 7, 1880-1900, 10.1175/MWR3154.1

McBeath, K., P.R. Field, R. Cotton, 2012: Using Operational Weather Radar to Assess High Resolution Numerical Weather Prediction over the British Isles for a Cold Air Outbreak Case Study. Submitted to QJRMS.

O'Dell, Christopher W. and Wentz, Frank J. and Bennartz, Ralf, 2008: Cloud liquid water path from satellite-based passive microwave observations: A new climatology over the global oceans. Journal of Climate, 21, 8, 1721-1739, 10.1175/2007JCLI1958.1

Smagorinsky J., 1963: General circulation experiments with the primitive equations. Part 1: the basic experiment. Monthly Weather Review, 91, 99-164.

Trenberth, K. E., and J. T. Fasullo, 2010: Simulation of Present-Day and Twenty-First-Century Energy Budgets of the Southern Oceans. Journal of Climate, 23, 440-454.

Tripoli, G. J. and Cotton, W. R. (1980). A numerical investigationof several factors contributing to the observed variable intensity of deep convection over south Florida. J. Appl. Meteorol., 19, 1037-1063.

Wacker, U and Potty, KVJ, Lüpkes, C and Hartmann, J and Raschendorfer, M, 2005: A case study on a polar cold air outbreak over fram strait using a mesoscale weather prediction model. Boundary-Layer Meteorology, 117, 2, 301-336, 10.1007/s10546-005-2189-1

Walters D.N. and coauthors, 2011: The Met Office Unified Model Global Atmosphere 3.0/3.1 and JULES Global Land 3.0/3.1 configurations, Geoscientific Model Development, 4, 4, 919-941, 10.5194/gmd-4-919-2011

Wentz, FJ and Spencer, RW, 1998. SSM/I rain retrievals within a unified all-weather ocean algorithm. Journal of the Atmospheric Sciences, 55, 9, 1613-1627, 10.1175/1520-0469(1998)055¡1613:SIRRWA¿2.0.CO;2

Westbrook, C. D., and A. J. Illingworth (2011), Evidence that ice forms primarily in supercooled liquid clouds at temperatures ¿ -27C, Geophys. Res. Lett., 38, L14808, doi:10.1029/2011GL048021.

Wielicki, B. A., B. R. Barkstrom, E. F. Harrison, R. B. Lee III, G. L. Smith, and J. E. Cooper, 1996: Clouds and

the Earth's Radiant Energy System (CERES): An Earth Observing System Experiment, Bull. Amer. Meteor. Soc., 77, 853-868.

Wilkinson, J. M., Wells, H., Field, P. R. and Agnew, P. (2012), Investigation and prediction of helicopter-triggered lightning over the North Sea. Met. Apps. doi: 10.1002/met.1314.

Wilson D. R., and S. P. Ballard, 1999: A microphysically based precipitation scheme for the UK Meteorological Office Unified Model. Quart. J. Roy. Meteor. Soc., 125, 1607-1636.
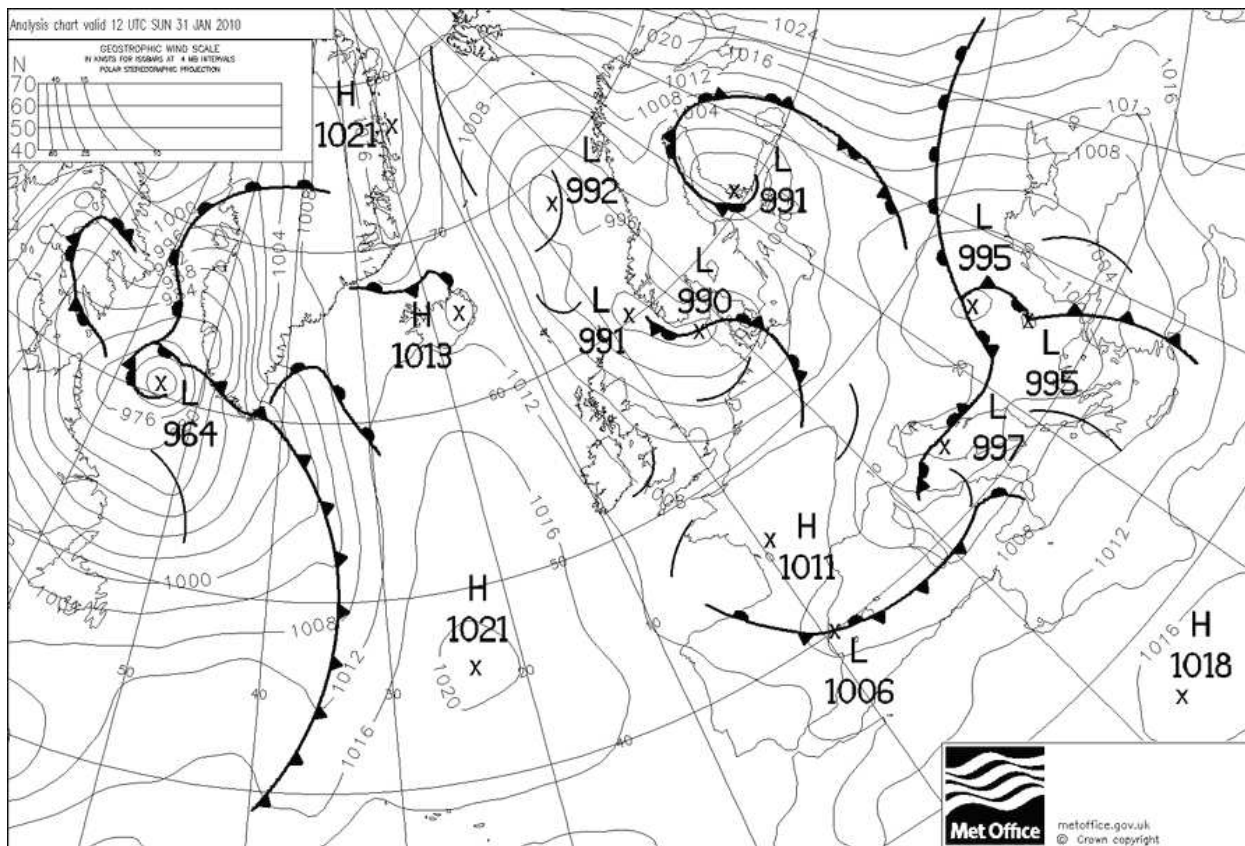
Figure 1. Analysis chart for 12 UTC 31st January 2010.
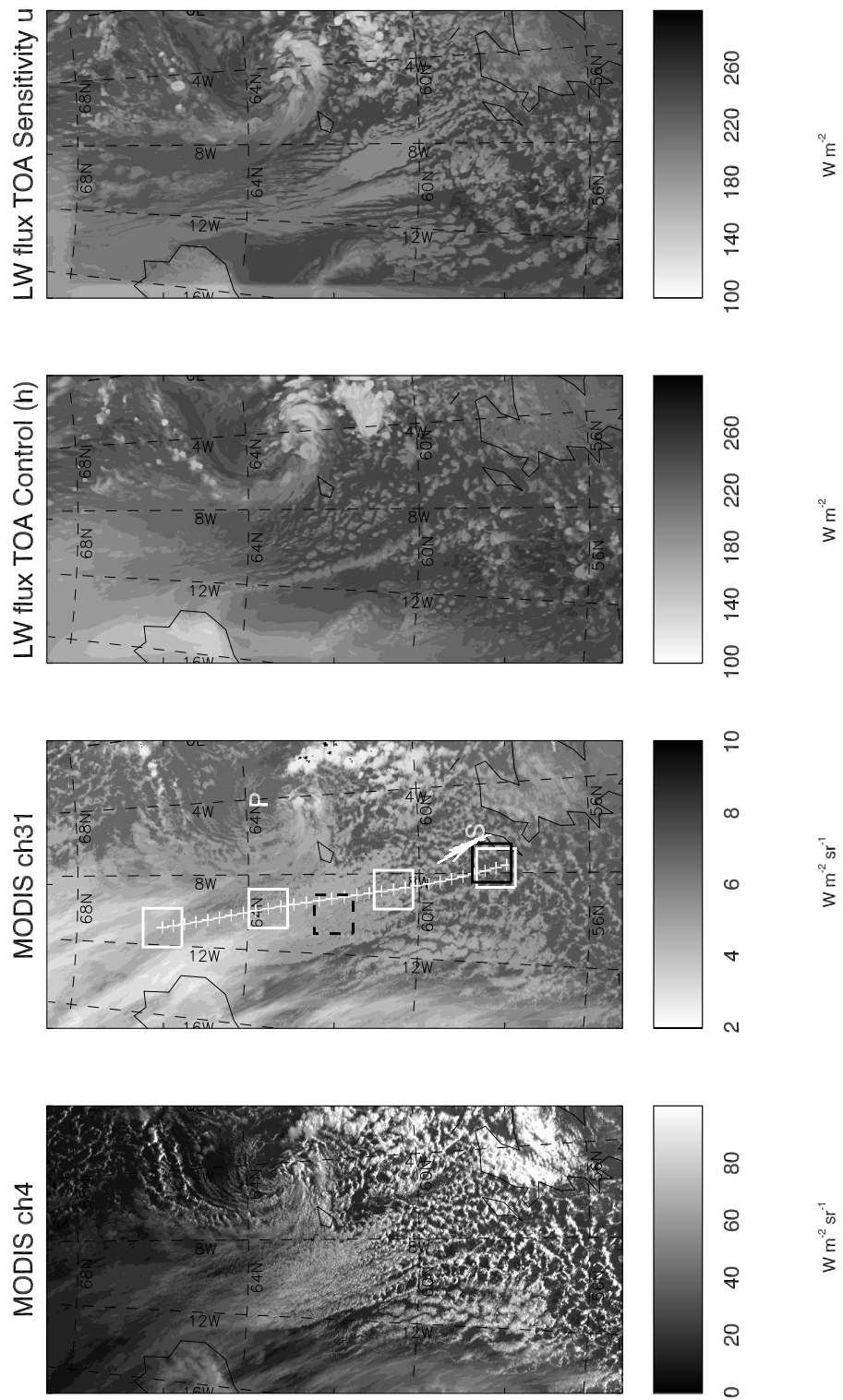
Figure 2. Comparison of MODIS channel 4 (visible, 550 nm, [a]) and 31 (infrared, 10 microns, [b]) [W m^{-2} sr^{-1}] with outgoing LW from the control model (dimsh, [c]) and sensitivity experiment (dimsu, [d]) [W m^{-2}]. Panel b contains the polar low feature indicated by a white 'P'. The sonde positions are very close to each other and are marked by a white 'S'. The aircraft runs used in the paper are marked by the white arcs. The Lagrangian trajectory is marked as a white line extending from 66N11W with plus marks half hour intervals from 0UTC to 15UTC. White boxes indicate the locations of the Lagrangian boxes used for figures 8,9. The black box indicates the region used for comparison with the aircraft data. The black dashed box indicates the region over which the MODIS retrievals of droplet number, cloud top temperature/pressure and cloud water path were averaged. The images are for 31st January 2010 12 UTC
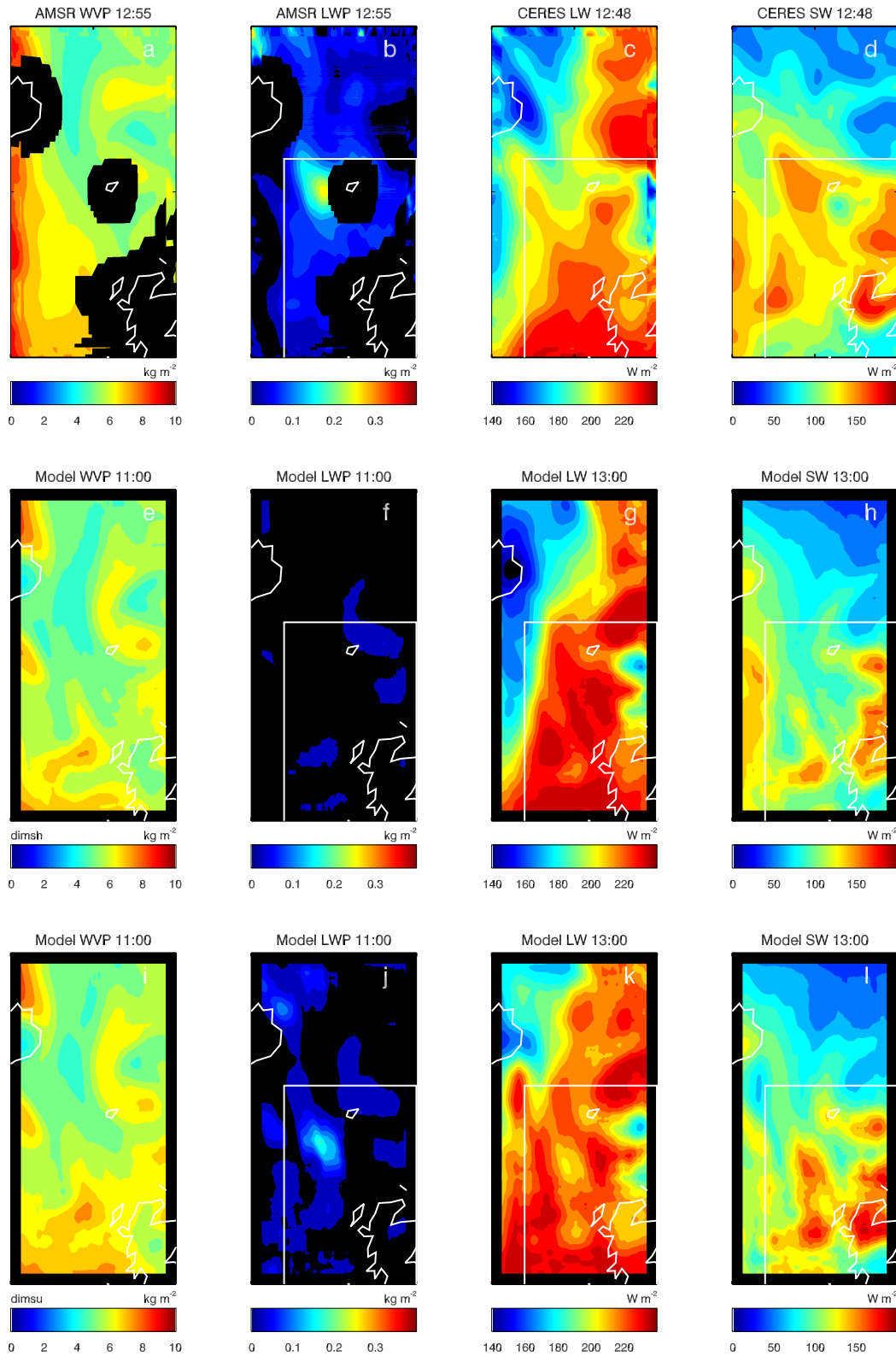
Figure 3. Comparison of satellite data (a-d) with the control (dimsh) model (e-h) and sensitivity experiment (dimsu). a,e,i integrated water vapour column, b,f,j liquid water path, c,g,k Long wave flux at the top of the atmosphere, d,h,l Short wave flux at the top of the atmosphere. All data have been smoothed by a 100km top-hat function. Black indicates zero value or missing data. White box indicates the region used to derive the average values presented in table 2.
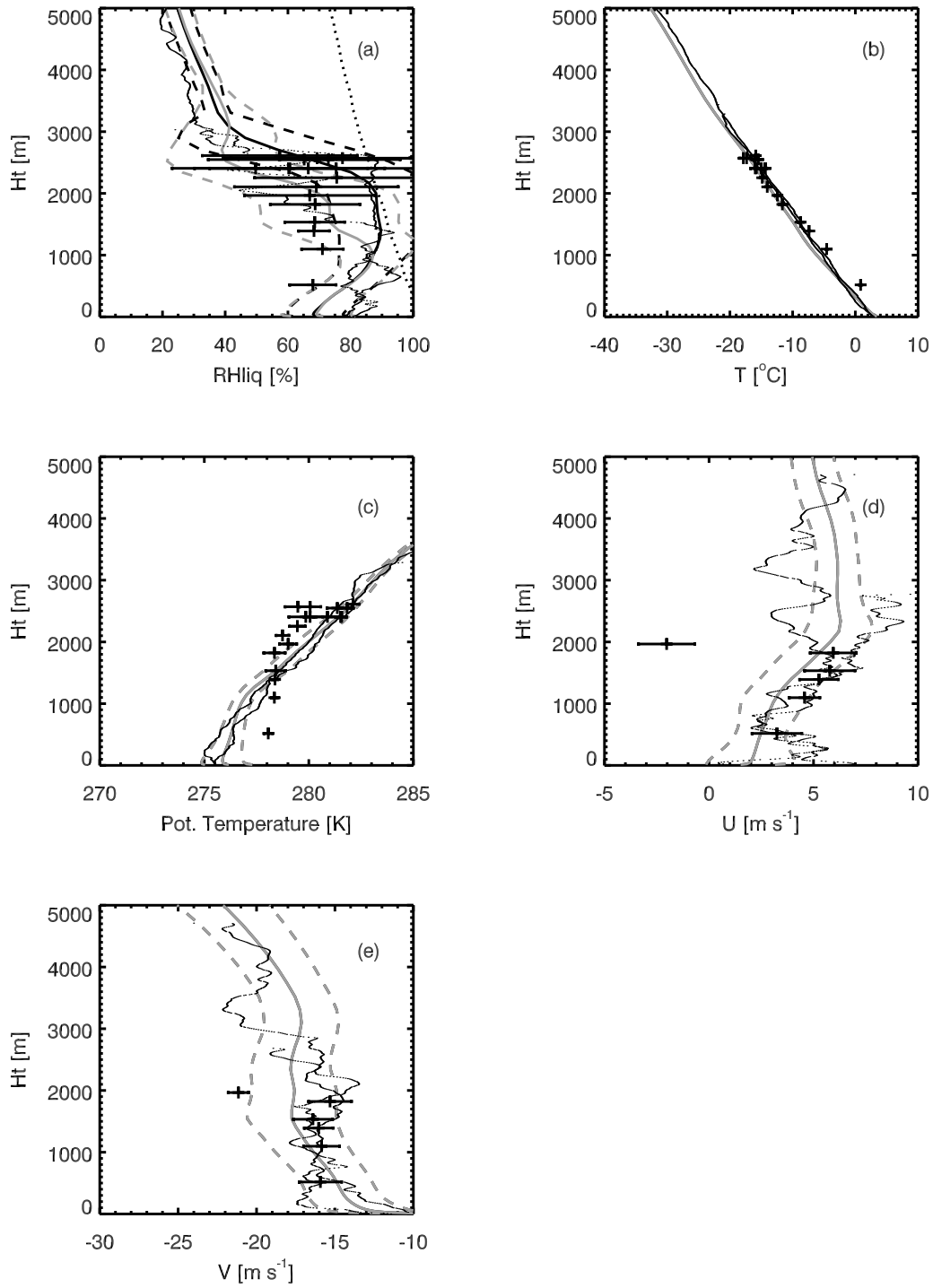
Figure 4. Height profile comparisons of dropsonde (thin dotted) and aircraft data (plus with variability bar) with control model (h) data (light grey) and sensitivity experiment (u) data (black): average from 100 km x 100 km box indicated in figure 2b (solid line and ±1 standard deviation (dashed lines (only for control). If only the grey solid line is visible, then the control and sensitivity profile is coincident. a) Relative humidity with respect to liquid (thick dotted line represents ice saturation). b) Temperature. c) Potential temperature. d) U wind. e) V wind. Model data 11 UTC, aircraft data 11-14 UTC.
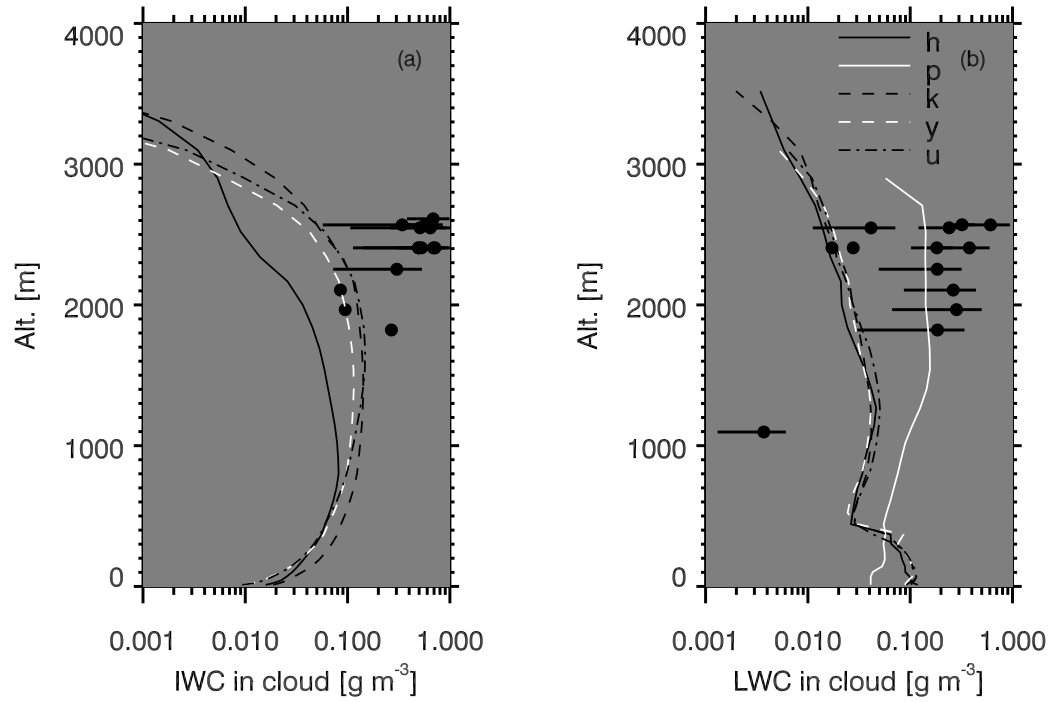
Figure 5. Height profile comparison of aircraft data (solid circles with 1 standard deviation variability bars) with 100 km x 100 km mean profiles for a subset of different configurations of the model (see table 1, h is control). a) In-cloud ice water contant, b) in-cloud liquid water content, c) ice cloud fraction, d) liquid cloud fraction
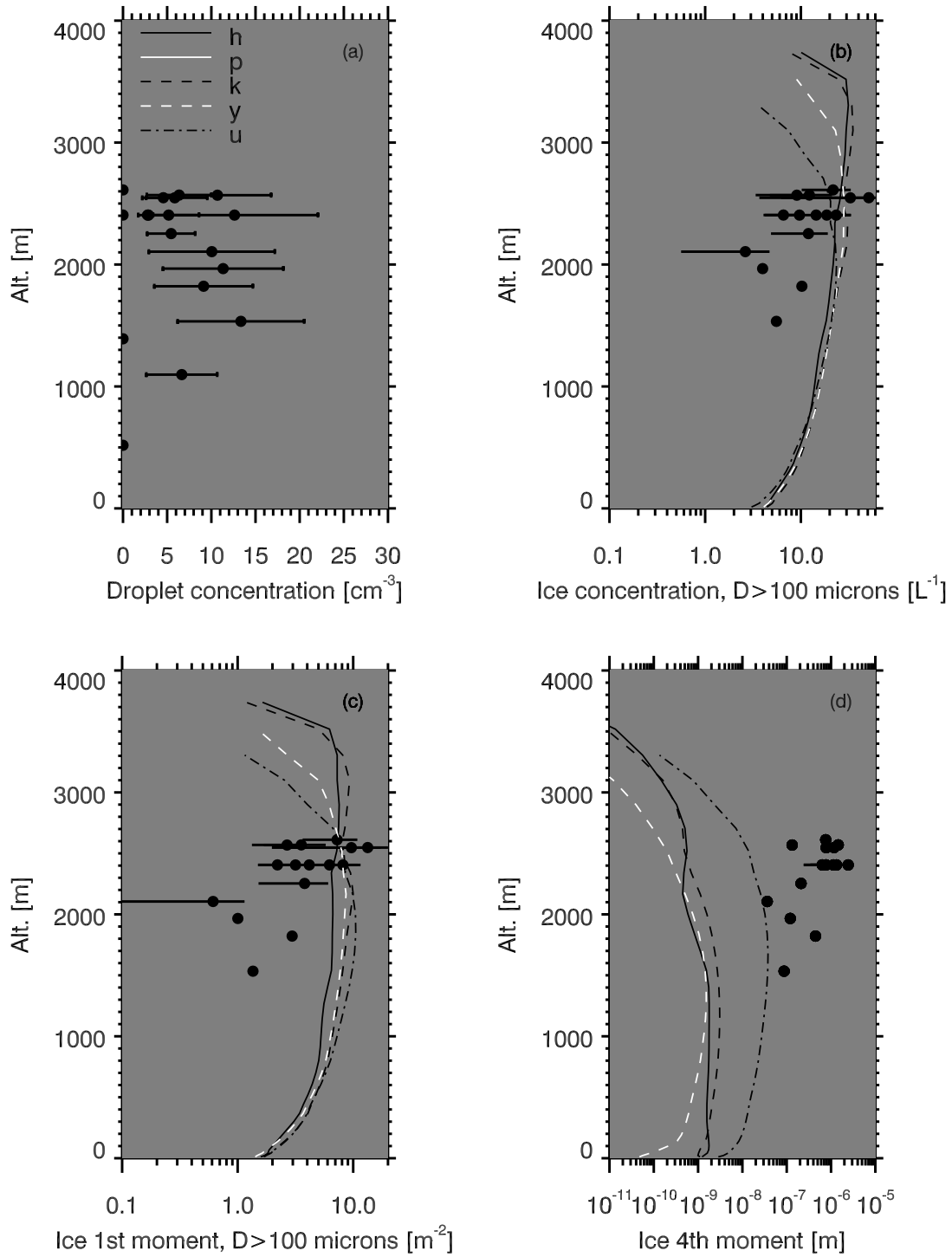
Figure 6. Same as fig. 5, but for a) droplet concentration, b) ice crystal concentration (D>100microns), c) first moment of ice size distribution (D>100 microns), d) fourth moment of ice size distribution (D>100microns). Control model: h, see table 1.
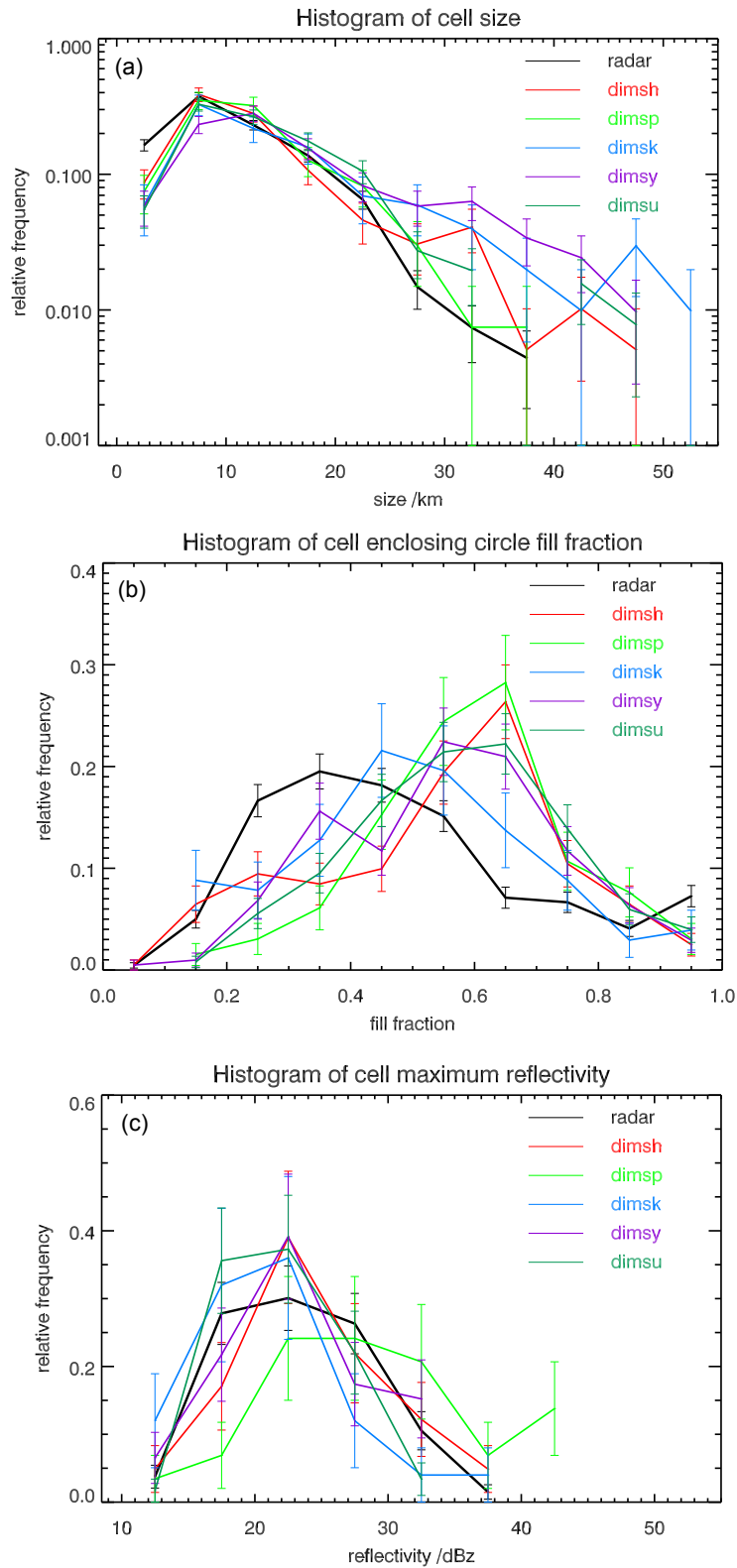
Figure 7. Comparison of convective cell statistics (mean and standard deviation) for a 10dBZ radar reflectivity contour at 2km altitude derived from the control (h) and a subset of sensitivity experiment model and radar data. Normalised histograms of a) convective cell size, b) convective cell fill fraction, c) maximum reflectivity in a cell.
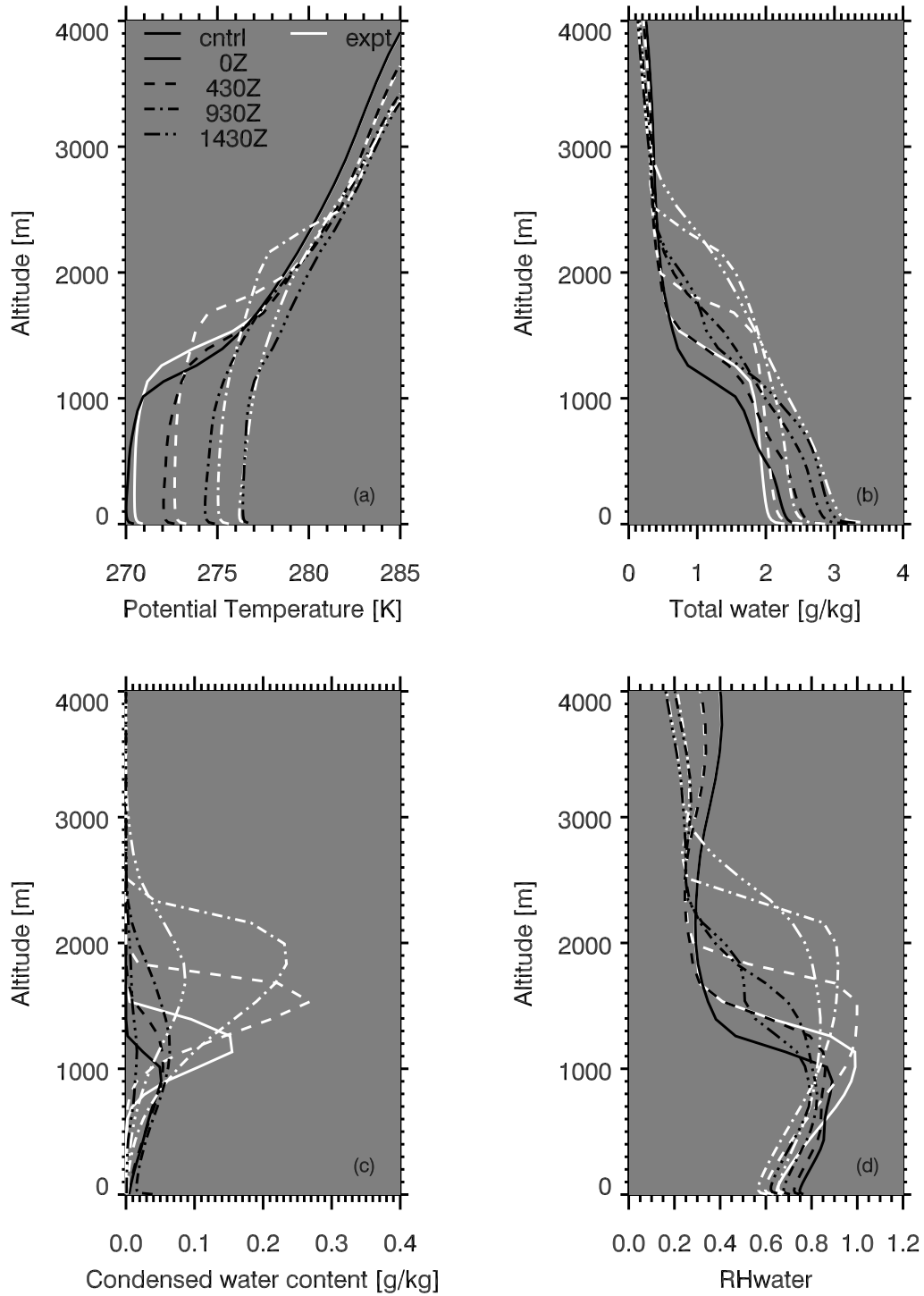
Figure 8. Boundary layer profiles comparing the control model (h) and one of the sensitivity experiments (u) at four times along the quasi-lagrangian trajectory highlighted in figure 2b. a) potential temperature, b) total water, c) condensed water content, d) relative humidity with respect to liquid.
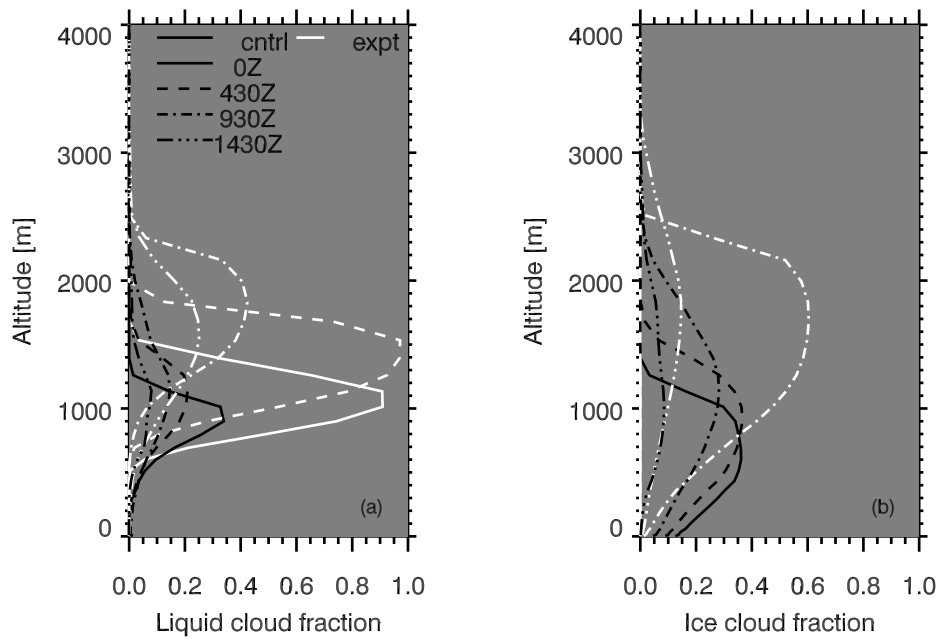
Figure 9. Same as fig. 8, but for a) liquid cloud fraction, b) ice cloud fraction. Cloud fraction is the fraction of grid boxes within the 100km x 100km box at each height that contain more than 10^{-8} kg kg $^{-1}$ of condensed water. Comparison of control model (h) with sensitivity experiment (u).